Design of a multi-resonator metamaterial for mitigating impact force

Q. Q. Li,[1] Z. C. He,[1,a)] Eric Li,[2,b)] and A. G. Cheng[1]

[1]*State Key Laboratory of Advanced Design and Manufacturing for Vehicle Body, Hunan University, Changsha 410082, P. R. China*

[2]*School of Science, Engineering & Design, Teesside University, Middleborough, UK*

In this paper, we propose a new multi-resonator metamaterial (MRM) for attenuating impact stress waves. Theoretical analyses show that the MRM has wider band gaps than those of a single-resonator metamaterial (SRM) and a dual-resonator metamaterial (DRM), and numerical studies are conducted to compare the performances of the MRM, SRM, and DRM in mitigating impact forces. The influences of the number of unit cells, the spring stiffnesses, and the resonator masses on the mitigation of impact force are analyzed by studying a one-dimensional impact wave model. In addition, the calculation results of a three-dimensional crash model clearly confirm the outstanding features of the MRM, which can provide a thin and light structure with a wider attenuation region of the frequency spectrum and a better mitigation effect of the impact force.

[a)]Electronic address: hezhicheng815@163.com

[b)]Electronic address: ericsg2012@gmail.com

I. INTRODUCTION

Metamaterials are artificial composite materials that have extraordinary physical properties not commonly possessed by natural materials. The metamaterials studied the most to date are electromagnetic metamaterials,[1–5] thermal metamaterials,[6–10] photonic metamaterials,[11,12] and acoustic metamaterials (AMs).[13–19] The design of these metamaterials overcomes the limitations of some natural laws by properly designing the internal mechanical structure instead of the chemical constituents.

Because of their exceptional ability to manipulate stress waves, AMs have attracted much research interest.[20–22] Cselyuszka et al.[23] presented a one-dimensional (1D) locally resonant AM with negative effective mass density. Assouar et al.[24] studied two plate-type AMs both theoretically and numerically and achieved high sound transmission loss with them. Wang[25] designed a new representative cell of an elastic metamaterial that could generate negative mass and negative modulus by translating and rotating the cell in a controlled manner. As well as the aforementioned theoretical studies, the potential engineering applications of AMs have been widely studied for acoustic attenuation,[26,27] noise control,[28–35] invisibility cloaking,[36] and energy absorption.[37,38]

The specially designed microstructure of an AM plays an important role in its performance. Therefore, there has been much research effort on AM microstructures for prohibiting/controlling the propagation of stress waves. Recently, a single-resonator metamaterial (SRM) was proposed for manipulating stress waves, and its performance has been studied theoretically, numerically, and

experimentally.[39–43] Zhou et al.[44] and Banerjee et al.[45] showed that an SRM can have two band gaps. The width of the second band gap is theoretically infinite and the first band gap can be divided into two parts, one due to the high effective mass and the other due to the negative effective mass (NEM). Liu et al.[46] discussed how the relevant parameters affect the band gap of the 1D single-resonator lattice system, and a method was provided for calculating the upper limit of the second stopband. It is worth noting that the unit cells in the 1D metamaterial proposed by Zhou et al.,[44] Banerjee et al.,[45] and Liu et al.[46] are connected by the external springs, and the second band gap and the lower part of the first band gap are produced by the presence of these springs.

Driven by these SRM features, Tan et al.[47,48] proposed a dual-resonator metamaterial (DRM) to further improve the attenuation of mechanical waves. Their theoretical and numerical results showed that a DRM has a wider band gap and better attenuates mechanical waves compared with an SRM. Despite a DRM being better at attenuating frequency spectra, its performance remains unsatisfactory for problems involving a wide frequency spectrum. To address practical requirements, there is a compelling need to design AM microstructures with wide and multiple band gaps.

In the present paper, a new multi-resonator metamaterial (MRM) is proposed. Unlike SRMs and DRMs, a unit cell of an MRM can be seen as the combination of a pair of DRM unit cells. In addition, the unit cells of the present lattice system are directly rigidly connected, avoiding the need for external springs. Therefore, the material studied herein is a special version of a 1D metamaterial. The present theoretical analyses show that an MRM has more band gaps and a wider frequency

region associated with NEM compared with SRMs and DRMs, which implies that an MRM can attenuate impact stress waves more effectively. Herein, we study quantitatively the performances of SRM, DRM, and MRM AMs at mitigating impact force. We use a 1D impact wave model to study how the number of unit cells, the spring stiffness, and the resonator mass influence the performances of an SRM, DRM, and MRM in attenuating stress waves. In addition, the results of the 1D impact wave model and a three-dimensional (3D) crash model reveal that an MRM with light and thin properties is always superior to an SRM and a DRM.

This paper is organized as follows. In Section II, we consider the designed AM microstructures theoretically. In Section III, we report on parametric studies of the three types of AM with the 1D impact wave model. In Section IV, we apply the 3D crash model to the three types of AM. Finally, we draw conclusions in Section V.

II. MICROSTRUCTURES OF ACOUSTIC METAMATERIALS

Herein, we study the attenuation effects of AMs based on their property of NEM. Single-resonator and dual-resonator microstructures[47,48] have been studied widely and have been shown to exhibit a stopband and NEM. In this section, we consider briefly the propagation and mitigation of a mechanical wave in a 1D lattice system with locally resonant microstructures.

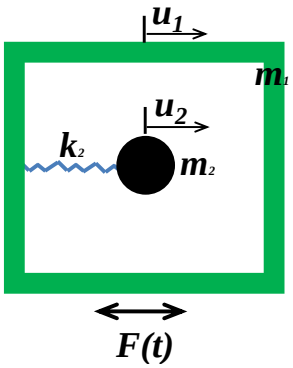

(a)

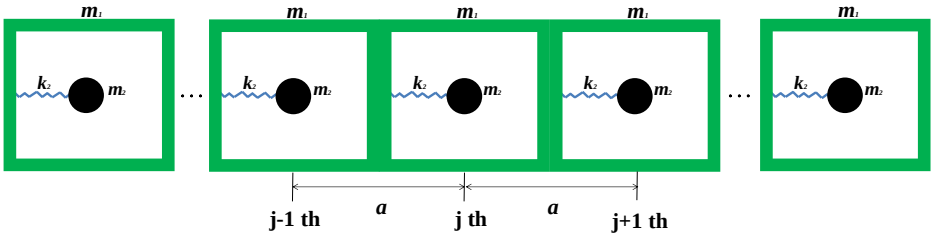

(b)

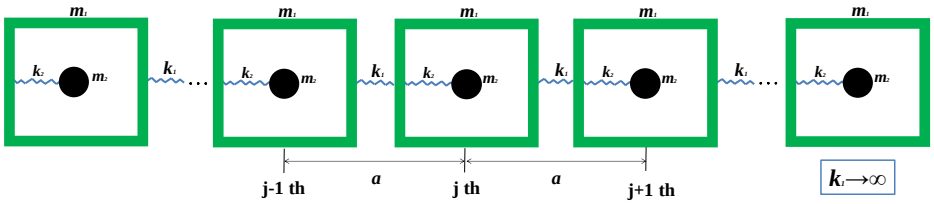

(c)

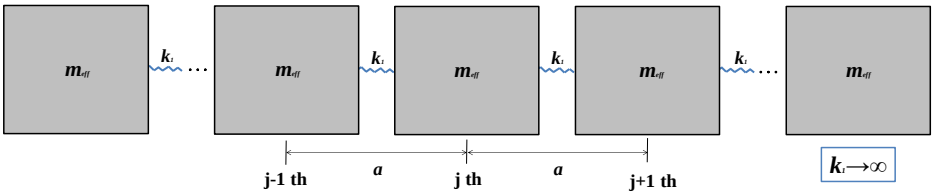

(d)

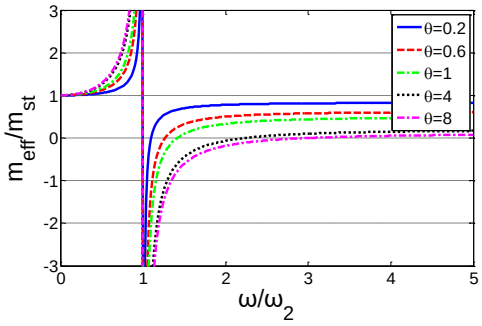

(e)

FIG. 1. (a) Microstructure of single-resonator metamaterial (SRM). (b) One-dimensional (1D) single-resonator lattice system. (c) 1D single-resonator lattice system with outer spring k_1 ($k_1 \to \infty$). (d) 1D monatomic lattice system with outer spring k_1 ($k_1 \to \infty$). (e) Curves of dimensionless effective mass for an SRM with different values of θ.

Figure 1(a) shows the single-resonator microstructure with external and internal masses m_1 and m_2, respectively, the displacements of which are u_1 and u_2, respectively. A linear spring of stiffness k_2 connects the internal and external masses. Figure 1(b) shows the 1D spring–mass lattice system comprising single-resonator microstructures. This SRM can be regarded as a spring–mass lattice system that is connected by outer springs of stiffness k_1 ($k_1 \to \infty$) as illustrated in Fig. 1(c). As such, the motions of the outer and inner masses of each unit cell can be assumed to satisfy periodic boundary conditions, allowing us to obtain the dispersion equation and the effective mass of the system. Based on Floquet–Bloch theory, the harmonic displacement of unit cell j+n is written as

$$u_a^{(j+\mathrm{n})} = \widehat{u}_a e^{i(qx+nqa-\omega t)}, \tag{1}$$

where $u_\alpha^{(j+n)}$ is the displacement of rigid mass α in unit cell j+n of the system, ω is the angular frequency, q is the wavenumber, $\widehat{u}_a$ is the displacement amplitude, and a is the lattice constant. For the 1D lattice system shown in Fig. 1(c), the equations for the rigid masses in unit cell j are obtained as follows based on Newton's Second Law:

$$m_1 \ddot{u}_1^{(j)} = k_1(u_1^{(j-1)} + u_1^{(j+1)} - 2u_1^{(j)}) + k_2(u_2^{(j)} - u_1^{(j)}), \tag{2}$$

$$m_2 \ddot{u}_2^{(j)} = k_2(u_1^{(j)} - u_2^{(j)}). \tag{3}$$

By substituting Eq. (1) into Eqs. (2) and (3), the dispersion relation of the lattice system can be calculated as

$$\cos qa = 1 - \frac{\delta}{2\theta}\frac{(\omega/\omega_2)^2[(\omega/\omega_2)^2 - (1+\theta)]}{(\omega/\omega_2)^2 - 1}, \tag{4}$$

where $\theta = m_2/m_1$ is the ratio of internal mass m_2 to external mass m_1, $\delta = k_2/k_1$ is the ratio of internal spring stiffness k_2 to external spring stiffness k_1; as $k_1 \to \infty$, $\delta \to 0$

and Eq. (4) can be written as $\cos(qa) \to 1$ and $q \to 0$.

As shown in Fig. 1(d), we regard this single-resonator lattice system as a monatomic lattice system whose effective mass m_{eff} is

$$m_{eff} = \frac{2k_1(1-\cos qa)}{\omega^2}. \tag{5}$$

Based on Eqs. (4) and (5), the effective mass of the single-resonator microstructure is therefore

$$m_{eff} = m_1 + \frac{\omega_2^2 m_2}{\omega_2^2 - \omega^2}, \tag{6}$$

the value of which clearly depends on the frequency ω_2. When the input frequency ω approaches the local frequency ω_2, the value of m_{eff} changes considerably. Finally, we obtain the dimensionless effective mass m_{eff}/m_{st}, which is the ratio of the effective mass m_{eff} to the static mass m_{st} of the microstructure:

$$\frac{m_{eff}}{m_{st}} = 1 + \frac{\theta}{1+\theta}\left[\frac{(\omega/\omega_2)^2}{1-(\omega/\omega_2)^2}\right]. \tag{7}$$

The parameter θ clearly has an important influence on the value of the dimensionless effective mass m_{eff}/m_{st}. The curve of m_{eff}/m_{st} against the dimensionless frequency ω/ω_2 is shown in Fig. 1(e), where there is a narrow frequency range in which m_{eff}/m_{st} is negative. Previous work[41] indicated that this frequency region associated with NEM corresponds to the attenuation band gap for mechanical wave propagation. NEM is produced when the input frequency reaches the local resonance frequency, and the band gap widens with increase of θ.

NEM is produced when the inequality $m_{eff}/m_{st} < 0$ is satisfied, leading to the inequality

$$\omega_2 \le \omega \le \sqrt{1+\theta}\omega_2 . \quad (8)$$

The local resonance frequency of an SRM clearly has an important effect on its dimensionless effective mass based on Eq. (8). Increasing that frequency broadens the frequency range associated with NEM. For example, for a mass ratio $\theta = 1$, the local resonance frequency is $\omega_2 = 500$ Hz and the frequency region associated with NEM is 500 Hz $< \omega <$ 707 Hz. Changing the local resonance frequency to $\omega_2 = 1{,}000$ Hz, the frequency region associated with NEM extends naturally to 1,000 Hz $< \omega <$ 1,414 Hz and a wider band gap is produced in the high-frequency domain.

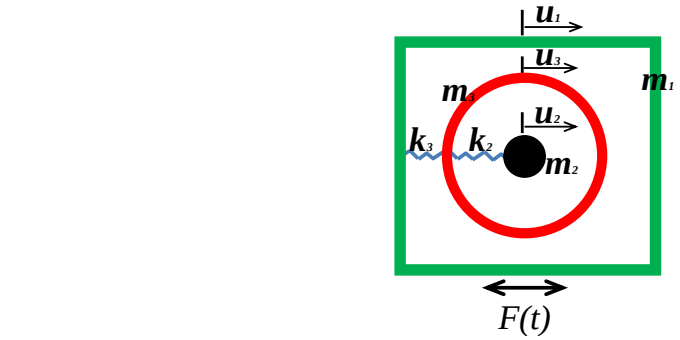

(a)

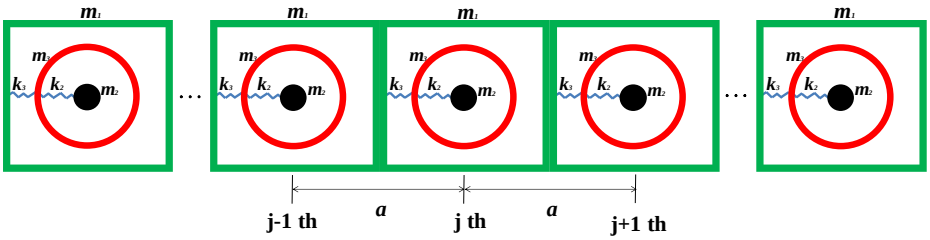

(b)

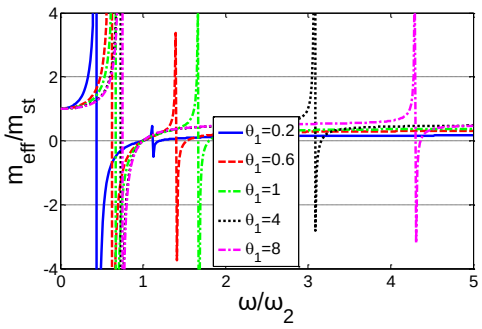

(c)

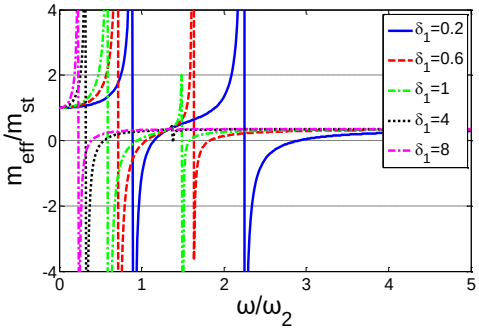

(d)

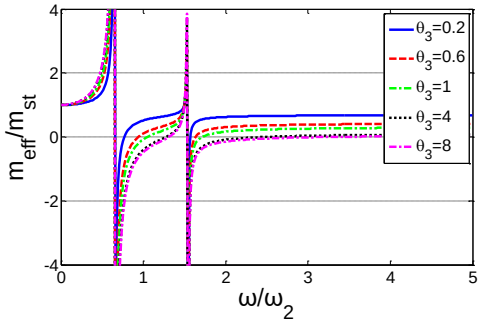

(e)

FIG. 2. (a) Microstructure of dual-resonator metamaterial (DRM). (b) 1D dual-resonator lattice system. Curves of dimensionless effective mass for a DRM with different values of (c) θ_1, (d) δ_1, and (e) θ_3.

Figure 2(a) shows the dual-resonator microstructure with three masses coupled by linear springs. The external, middle, and internal resonator masses are m_1, m_3, and m_2, respectively, with displacements u_1, u_3, and u_2, respectively, and k_3 and k_2 are the spring stiffnesses. The 1D dual-resonator lattice system comprising dual-resonator microstructures is shown in Fig. 2(b). Based on the same principle as that applied to Fig. 1, the equations of motion for unit cell j are

$$m_1\ddot{u}_1^{(j)} = k_1(u_1^{(j-1)} + u_1^{(j+1)} - 2u_1^{(j)}) + k_3(u_3^{(j)} - u_1^{(j)}), \tag{9}$$

$$m_1\ddot{u}_2^{(j)} = k_2(u_3^{(j)} - u_2^{(j)}), \tag{10}$$

$$m_3\ddot{u}_3^{(j)} = k_2(u_2^{(j)} - 2u_3^{(j)}) + k_3(u_1^{(j)} - u_3^{(j)}). \tag{11}$$

Similar to the single-resonator microstructure, the dimensionless effective mass m_{eff}/m_{st} of the dual-resonator microstructure is obtained as

$$\frac{m_{eff}}{m_{st}} = \frac{\theta_1}{\theta_1+\theta_2+\theta_1\theta_2} + \frac{\theta_2}{\theta_1+\theta_2+\theta_1\theta_2}\left[\frac{1+\theta_1\text{-}(\omega/\omega_2)^2}{[1-(\omega/\omega_2)^2][1+\delta_1-(\delta_1/\theta_1)(\omega/\omega_2)^2]-\delta_1}\right], \tag{12}$$

where $\theta_1 = m_2/m_3$ is the ratio of internal mass m_2 to middle mass m_3, $\theta_2 = m_2/m_1$ is the ratio of internal mass m_2 to external mass m_1, $\theta_3 = m_3/m_1$ is the ratio of middle mass m_3 to outer mass m_1, $\delta_1 = k_2/k_3$ is the ratio of internal spring stiffness k_2 to middle spring stiffness k_3, and $\omega_2 = \sqrt{k_2/m_2}$ is the local resonance frequency of internal mass m_2.

Figures 2(c)–2(e) show how θ_1, θ_3, and δ_1 influence the dimensionless effective mass m_{eff}/m_{st}. The DRM clearly has a wider frequency range associated with NEM than that of the SRM because of the double band gaps of the former. As shown in Fig. 2(c), the band-gap region widens as θ_1 is increased, with the widening of the

second band gap being particularly obvious. However, Fig. 2(d) shows that the effect of δ_1 is opposite to that of θ_1: the frequency region associated with NEM narrows as δ_1 is increased (i.e., either k_2 is increased of k_3 is decreased). In addition, as shown in Fig. 2(e), increasing parameter θ_3 widens these two band gaps simultaneously.

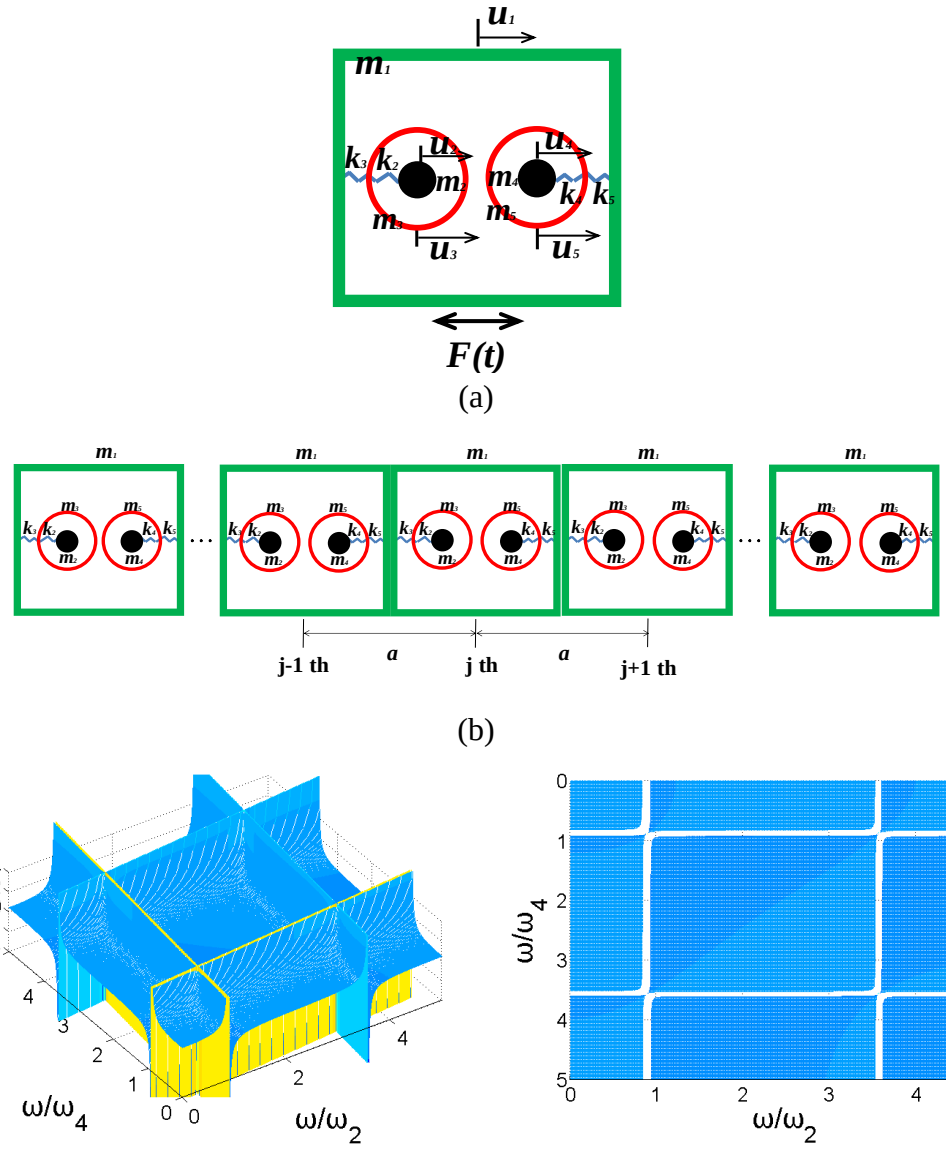

(a)

(b)

(c) (d)

FIG. 3. (a) Multi-resonator microstructure. (b) 1D multi-resonator lattice system. Three-dimensional (3D) graph of dimensionless effective mass against dimensionless frequencies: (c) global view; (d) bottom view.

As shown in Fig. 3(a), we propose a new multi-resonator microstructure that is

the linear combination of two dual-resonator microstructures. The new model contains five rigid masses, namely internal masses m_2 and m_4, middle masses m_3 and m_5, and outer mass m_1, with displacements u_2, u_4, u_3, u_5, and u_1, respectively. The spring stiffnesses are k_2, k_3, k_4, and k_5. Figure 3(b) shows the 1D multi-resonator lattice system comprising multi-resonator microstructures, and the equations of motion of the rigid masses for unit cell j are

$$m_1\ddot{u}_1^{(j)} = k_1(u_1^{(j-1)} + u_1^{(j+1)} - 2u_1^{(j)}) + k_3(u_3^{(j)} - u_1^{(j)}) + k_5(u_5^{(j)} - u_1^{(j)}), \tag{13}$$

$$m_1\ddot{u}_2^{(j)} = k_2(u_3^{(j)} - u_2^{(j)}), \tag{14}$$

$$m_2\ddot{u}_3^{(j)} = k_3(u_1^{(j)} - u_3^{(j)}) + k_2(u_2^{(j)} - u_3^{(j)}), \tag{15}$$

$$m_4\ddot{u}_4^{(j)} = k_4(u_4^{(j)} - u_5^{(j)}), \tag{16}$$

$$m_5\ddot{u}_5^{(j)} = k_5(u_1^{(j)} - u_5^{(j)}) + k_4(u_4^{(j)} - u_5^{(j)}). \tag{17}$$

Analogously, the dimensionless effective mass m_{eff}/m_{st} of the multi-resonator microstructure is given as

$$\begin{aligned}\frac{m_{eff}}{m_{st}} = {} & \frac{1}{1+(\theta_2+1)\gamma_3+(1+\theta_4)\gamma_5} \\ & + \frac{\gamma_3}{1+(\theta_2+1)\gamma_3+(1+\theta_4)\gamma_5}\frac{((\omega/\omega_2)^2-\theta_2-1)\theta_2}{\delta_2(\omega/\omega_2)^2(\theta_2-(\omega/\omega_2)^2+1)+\theta_2((\omega/\omega_2)^2-1)} \\ & + \frac{\gamma_5}{1+(\theta_2+1)\gamma_3+(1+\theta_4)\gamma_5}\frac{((\omega/\omega_4)^2-\theta_4-1)\theta_4}{\delta_4(\omega/\omega_4)^2(\theta_4-(\omega/\omega_4)^2+1)+\theta_4((\omega/\omega_4)^2-1)},\end{aligned} \tag{18}$$

where $\gamma_2 = m_2/m_1$ is the ratio of the left inner mass m_2 to external mass m_1, $\gamma_3 = m_3/m_1$ is the ratio of the left middle mass m_3 to external mass m_1, $\gamma_4 = m_4/m_1$ is the ratio of the right inner mass m_4 to outer mass m_1, $\gamma_5 = m_5/m_1$ is the ratio of the right middle mass m_5 to external mass m_1, $\theta_2 = m_2/m_3$ is the ratio of the left internal mass m_2 to the left middle mass m_3, $\delta_2 = k_2/k_3$ is the ratio of the left internal spring stiffness k_2 to the left middle spring stiffness k_3, $\theta_4 = m_4/m_5$ is the ratio of the right internal mass m_4 to

the right middle mass m_5, and $\delta_4 = k_4/k_5$ is the ratio of the right internal spring stiffness k_4 to the right middle spring stiffness k_5.

Figures 3(c) and 3(d) show global and bottom views, respectively, of the 3D graph of dimensionless effective mass m_{eff}/m_{st} against dimensionless frequencies ω/ω_2 and ω/ω_4. There are clearly four band gaps in these two pictures, with the first band gaps on the ω/ω_2 and ω/ω_4 axes shown in yellow to distinguish them from the second band gaps on those two axes. Furthermore, because of its multiple band gaps, we expect that the proposed MRM can achieve a wider frequency region associated with NEM compared with an SRM and a DRM. The MRM microstructure involves six parameters, but only θ_2, δ_2, and γ_3 are studied in this section because of the symmetry of this microstructure. Figure 4 shows two-dimensional (2D) plots of m_{eff}/m_{st} against ω/ω_2 for the MRM to allow is to evaluate how these parameters affect these band gaps. From Fig. 4(a), increasing θ_2 (i.e., either increasing m_2 or decreasing m_3) widens the band gaps on the ω/ω_2 axis, and this increase is particularly pronounced for the second band gap. By contrast, Fig. 4(b) shows that increasing δ_2 narrows the frequency region associated with NEM on the ω/ω_2 axis, and continuing to increase δ_2 causes the second band gap to disappear. Figure 4(c) shows the positive influence of parameter γ_3 on these two band gaps: as γ_3 is increased, the two band gaps widen considerably. Therefore, the above parametric analyses imply that AMs with better attenuation can be achieved by the proper design of the spring stiffness and the rigid mass.

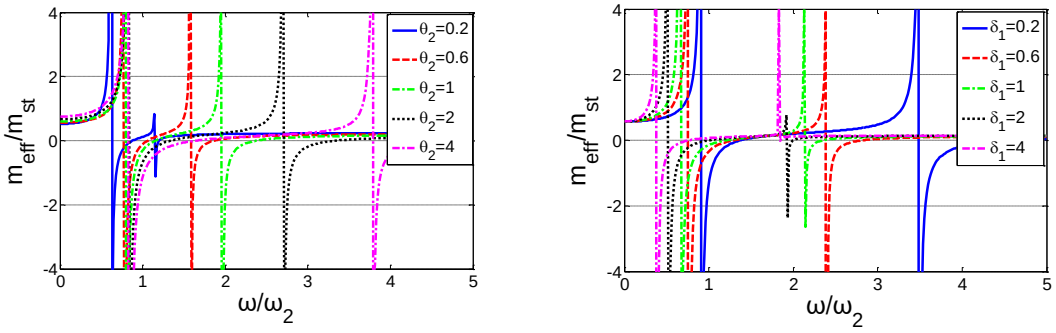

(a) (b)

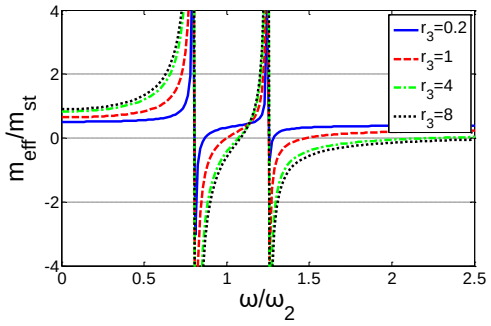

(c)

FIG. 4. Two-dimensional (2D) plots of dimensionless effective mass against dimensionless frequency ω/ω_2 for a multi-resonator metamaterial (MRM) with different values of (a) θ_2, (b) δ_1, and (c) r_3.

III. ONE-DIMENSIONAL IMPACT WAVE MODEL

In this section, we use a 1D impact wave model to study the attenuation effects of AMs. As shown in Fig. 5(a), the 1D model is divided into mediums 1, 2, and 3, with medium 3 being an AM model (SRM, DRM, or MRM) as shown in Fig. 5(b). The impact wave specified by

$$\begin{aligned} F &= F_{\max} e^{-\frac{t-t_0}{t_d}} \quad t \geq t_0 \\ F &= 0 \qquad\qquad t < 0 \end{aligned} \tag{19}$$

is applied to the front of medium 1, where F_{max} is the peak impact force, t_0 = 0.5 ms, and t_d = 0.1 ms. The duration time of the entire wave is 6 ms. We used the commercial software LSDYNA to conduct the analysis, selecting the impact force of element 20 in medium 2 as the output response. The impact force and its frequency spectrum obtained with a fast Fourier transform are shown in Fig. 6, which shows that the peak impact force is 303 N and the frequency range is 0–5,000 Hz.

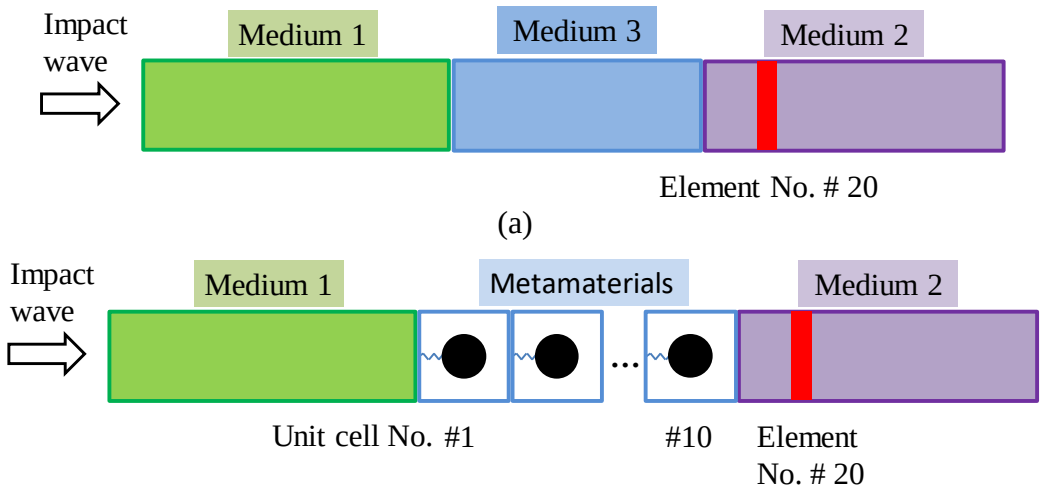

FIG. 5. 1D impact wave model: (a) schematic; (b) with medium 3 represented as an AM.

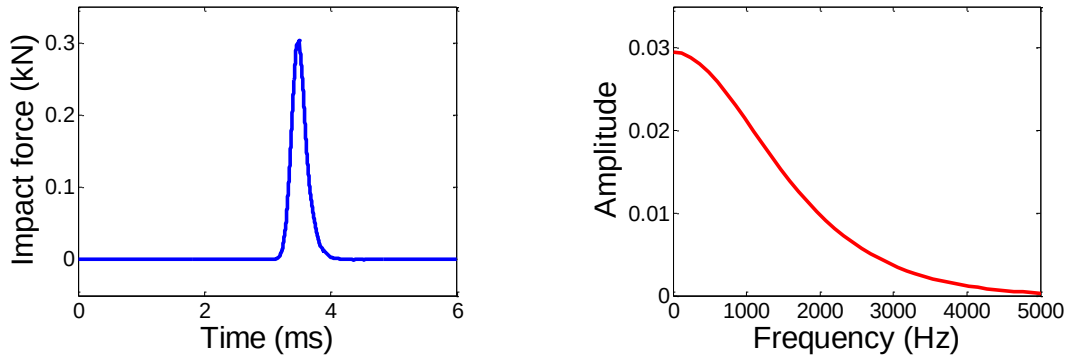

(a) (b)

FIG. 6. Impact force: (a) time series; (b) frequency spectrum of (a) obtained with a fast Fourier transform.

We discuss how the specific number of unit cells and the spring stiffnesses influence the AM performance. The rigid masses, spring stiffnesses, and local resonance frequencies in one unit cell of the SRM, DRM, and MRM are listed in Table 1. It is worth noting that unlike the SRM and DRM, the MRM has two local resonance frequencies due to its two internal resonator masses m_2 and m_4 in one unit cell. There are five groups of parameters in Table 1 for all the AMs. The number N of unit cells in each group is presented in the final column of the table. The internal

masses and outer mass in one unit cell of all the AM models are set as 0.03 kg, which means that the mass ratio θ of the SRM and those of θ_1 and θ_3 of the DRM and θ_2, γ_3, θ_4, and γ_5 of the MRM are all equal to unity. Because of the fixed rigid masses and mass ratios, it is the spring stiffnesses in Table 1 that determine the overall performance of each AM.

Table 1. Parameters of one unit cell in three different AM models.

		m_1, m_2, m_3, m_4, m_5 (kg)	k_2, k_3, k_4, k_5 (kN/mm)	ω_2, ω_4 (Hz)	N
SRM	group 1	0.03, 0.03, -, -, -	0.296, -, -, -	500, -	1
	group 2	0.03, 0.03, -, -, -	0.296, -, -, -	500, -	5
	group 3	0.03, 0.03, -, -, -	0.296, -, -, -	500, -	10
	group 4	0.03, 0.03, -, -, -	4.747, -, -, -	2000, -	5
	group 5	0.03, 0.03, -, -, -	14.508, -, -, -	3000, -	5
DRM	group 1	0.03, 0.03, 0.03, -, -	0.296, 2.665, -, -	500, -	1
	group 2	0.03, 0.03, 0.03, -, -	0.296, 2.665, -, -	500, -	5
	group 3	0.03, 0.03, 0.03, -, -	0.296, 2.665, -, -	500, -	10
	group 4	0.03, 0.03, 0.03, -, -	0.296, 4.737, -, -	500, -	5
	group 5	0.03, 0.03, 0.03, -, -	0.296, 14.508, -, -	500, -	5
MRM	group 1	0.03, 0.03, 0.03, 0.03, 0.03	0.296, 2.665, 1.184, 4.737	500, 1000	1
	group 2	0.03, 0.03, 0.03, 0.03, 0.03	0.296, 2.665, 1.184, 4.737	500, 1000	5
	group 3	0.03, 0.03, 0.03, 0.03, 0.03	0.296, 2.665, 1.184, 4.737	500, 1000	10
	group 4	0.03, 0.03, 0.03, 0.03, 0.03	0.296, 4.737, 1.184, 7.402	500, 1000	5
	group 5	0.03, 0.03, 0.03, 0.03, 0.03	0.296, 7.402, 1.184, 14.508	500, 1000	5

Figure 7 and Table 2 compare the results for the frequency spectrum and impact force of all the AM models. It is worth noting the considerable drop in spectral amplitude at the local resonance frequencies of each AM model in Fig. 7(a). Figure 7(b) shows how each AM mitigates the impact force. In groups 1, 2, and 3, the number of unit cells in each model is changed from one to 10. The maximum impact forces for the SRM, DRM, and MRM models are reduced from 0.302 kN to 0.233 kN,

from 0.285 kN to 0.176 kN, and from 0.263 kN to 0.120 kN, respectively. In addition, in the frequency range associated with attenuation, the spectral amplitude decreases rapidly with the number of unit cells. Therefore, both the spectral amplitude and the peak impact force are reduced considerably by increasing the number of unit cells.

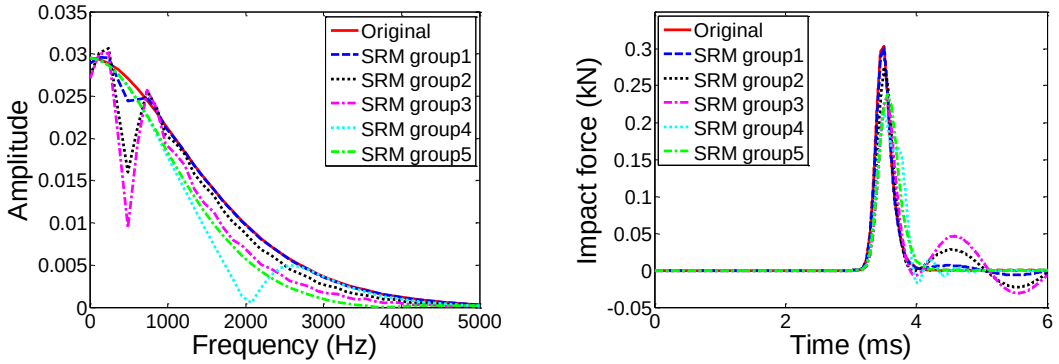

(a1) (b1)

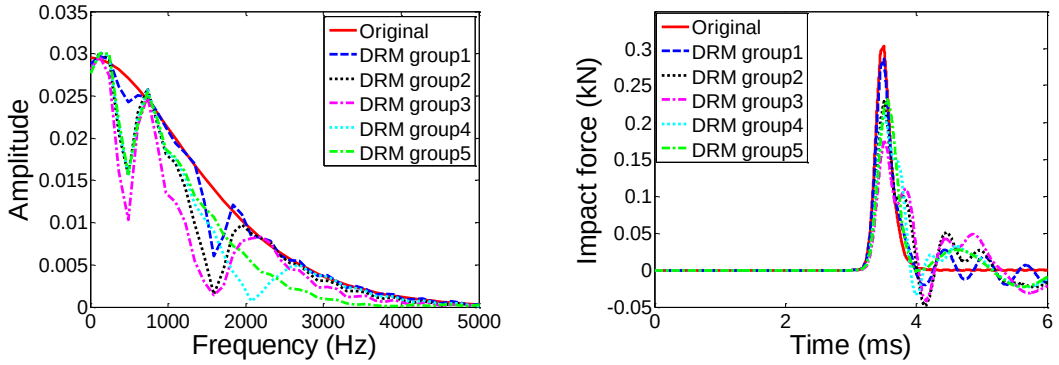

(a2) (b2)

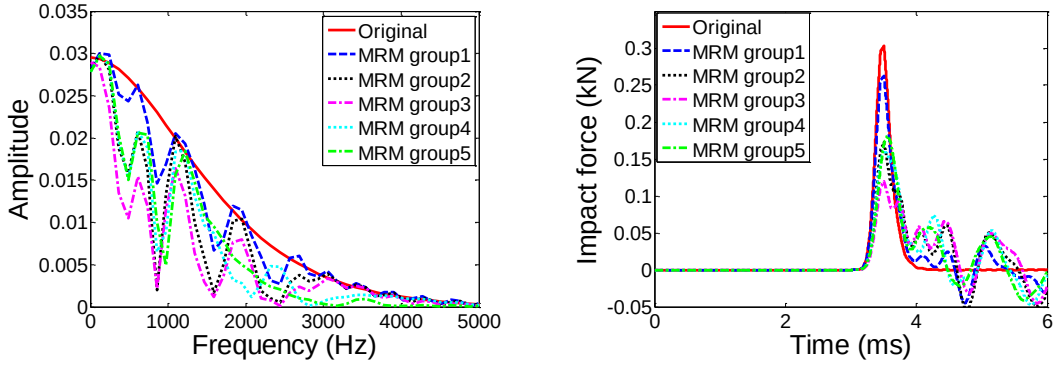

(a3) (b3)

FIG. 7. (a) Attenuation of frequency spectrum with different acoustic metamaterials (AMs). (b) Mitigation of impact force with different AMs.

For groups 2, 4, and 5 in Fig. 7(b) and Table 2, the mitigation of impact force in all the AM models increases initially and then decreases upon increasing the SRM local resonance frequency and decreasing the DRM spring stiffness ratio δ_1 and the MRM spring stiffness ratios δ_2 and δ_4. The main reason for this phenomenon is that the frequency range of this impact-force curve is 0–5,000 Hz, and its spectral amplitude decreases rapidly as the frequency increases. Therefore, the spectral amplitude in the high-frequency region is very small. For groups 2 and 4 in Fig. 7(a), the attenuation range of the SRM frequency spectrum broadens as the local resonance frequency is increased. In addition, the second DRM band gap and the third and fourth MRM band gaps widen as the DRM spring stiffness ratio δ_1 and the MRM spring stiffness ratios δ_2 and δ_4 are decreased. Thus, the attenuation effects of these three AM models increase. However, as the local SRM resonance frequency is increased continuously and the DRM and MRM spring stiffness ratios are decreased continuously, the attenuation region reaches the high-frequency region for groups 4 and 5 as shown in Fig. 7(a). The SRM band gap (the only one), the second DRM band gap (of two), and the third and fourth MRM band gaps (of four) approach 5,000 Hz, and the attenuation effects of these AMs are reduced despite their large attenuation ranges in the high-frequency region. Therefore, the proper design of the spring stiffness can improve the SRM, DRM, and MRM performances. In addition, the peak impact force achieved with 10 MRM unit cells is 0.120 kN. With the same 10 unit cells, the peak SRM and DRM impact forces are 0.233 kN and 0.176 kN, respectively. Therefore, it is clear that the MRM outperforms both the SRM and the DRM.

In Table 3, the spring stiffness ratios (DRM and MRM), the local resonance frequency, and the number of unit cells are the same for each AM model. The mass ratios θ (SRM), θ_1 and θ_3 (DRM), and θ_2, γ_3, θ_4, and γ_5 (MRM) for group 2 are larger than those for group 1. In each AM model, the internal resonator mass for group 3 is 0.06 kg (twice that for group 1).

Table 2. Maximum impact forces for three different AM models.

	Original (kN)	SRM (kN)	DRM (kN)	MRM (kN)
group 1	0.303	0.302	0.285	0.263
group 2		0.275	0.228	0.172
group 3		0.233	0.176	0.120
group 4		0.213	0.212	0.163
group 5		0.238	0.231	0.182

Table 3. The spring stiffnesses and rigid masses in one unit cell of these three AM models.

		m_1, m_2, m_3, m_4, m_5 (kg)	k_2, k_3, k_4, k_5 (kN/mm)	ω_2, ω_4 (Hz)	N
SRM	group 1	0.03, 0.03, -, -, -	1.184, -, -, -	1000, -	5
	group 2	0.02, 0.04, -, -, -	1.579, -, -, -	1000, -	5
	group 3	0.03, 0.06, -, -, -	2.369, -, -, -	1000, -	5
DRM	group 1	0.03, 0.03, 0.03, -, -	0.296, 2.665, -, -	500, -	5
	group 2	0.01, 0.03, 0.05, -, -	0.493, 4.439, -, -	500, -	5
	group 3	0.03, 0.06, 0.06, -, -	0.592, 5.330, -, -	500, -	5
MRM	group 1	0.03, 0.03, 0.03, 0.03, 0.03	0.296, 2.665, 1.184, 4.737	500, 1000	5
	group 2	0.01, 0.03, 0.04, 0.03, 0.04	0.493, 4.439, 1.974, 7.898	500, 1000	5
	group 3	0.03, 0.06, 0.06, 0.06, 0.06	0.592, 5.330, 2.369, 9.475	500, 1000	5

The results for frequency spectrum and impact force are shown in Fig. 8 and Table 4, respectively. These numerical results agree very well with the theoretical ones in Figs. 1(b), 1(d), and 1(f) and Figs. 4(a) and 4(c). First, with the same total static mass, Fig. 8 and Table 4 show an obviously improved mitigation of impact

force for groups 1 and 2 as the mass ratios increase for all the AM models. The maximum impact forces with the SRM, DRM, and MRM models are reduced from 0.252 kN to 0.246 kN, from 0.228 kN to 0.214 kN, and from 0.172 kN to 0.163kN, respectively. Second, groups 1 and 3 indicate a positive relationship between the internal resonator mass and the attenuation effect. For each AM model, the mitigations of the frequency spectrum and the impact force improve considerably as the resonator mass is increased. In addition, the minimum peak impact force of 0.118 kN is achieved by the MRM, which obviously outperforms the SRM and DRM with the same five unit cells.

Table 4. Maximum impact forces with each AM model.

	Original (kN)	SRM (kN)	DRM (kN)	MRM (kN)
group 1	0.303	0.252	0.228	0.172
group 2		0.246	0.214	0.163
group 3		0.224	0.185	0.118

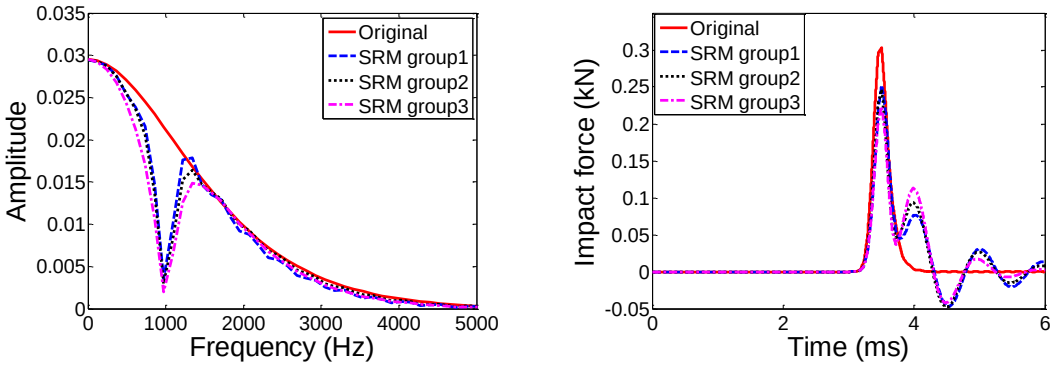

(a1) (b1)

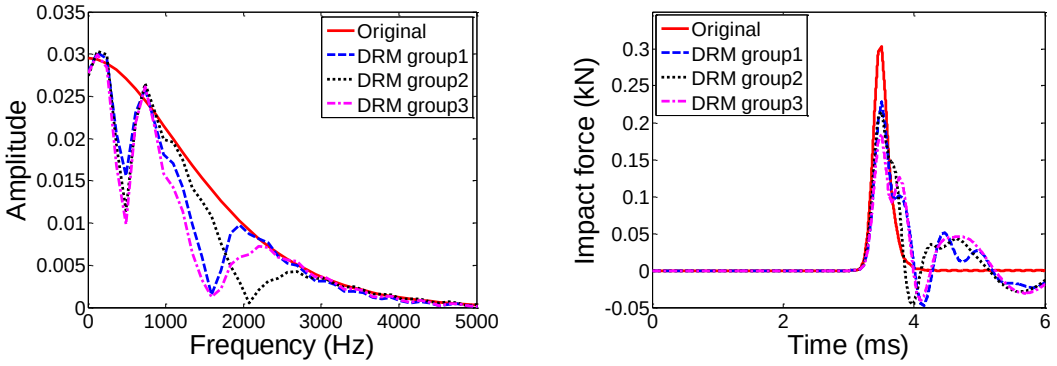

(a2) (b2)

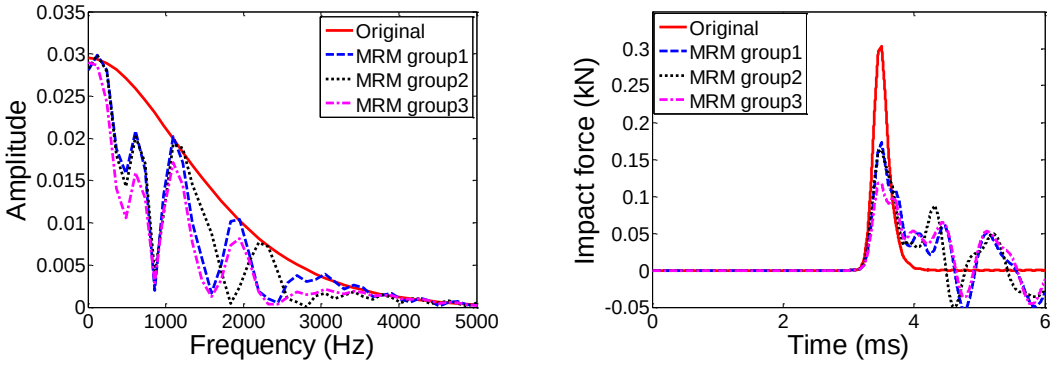

(a3) (b3)

FIG. 8. (a) Attenuation of frequency spectrum with different AMs. (b) Mitigation of impact force with different AMs.

One MRM unit cell can be seen as the linear combination of either two DRM unit cells or four SRM unit cells. For comparative analyses, we use three AM models: one comprising one MRM unit cell, one comprising two DRM unit cells, and one comprising four SRM unit cells. The detailed parameters for the one MRM unit cell, the two DRM unit cells, and the four SRM unit cells are presented in Table 5. Figure 9 and Table 6 show the results for the frequency spectrum and impact force, respectively, with these three AM models.

Table 5. Parameters for one MRM unit cell, two DRM unit cells, and four SRM unit cells.

	m_1, m_2, m_3, m_4, m_5 (kg)	k_2, k_3, k_4, k_5 (kN/mm)	ω_2, ω_4 (Hz)	N
MRM	0.03, 0.03, 0.03, 0.03, 0.03	0.296, 2.665, 1.184, 4.737	500, 1000	1
	m_1, m_2, m_3, m_2, m_3 (kg)	k_2, k_3, k_2, k_3 (kN/mm)	ω_2, ω_2 (Hz)	N
DRM	0.03, 0.03, 0.03, 0.03, 0.03	0.296, 2.665, 1.184, 4.737	500, 1000	2
	m_1, m_2, m_2, m_2, m_2 (kg)	k_2, k_2, k_2, k_2 (kN/mm)	ω_2, ω_2, ω_2, ω_2, (Hz)	N
SRM	0.03, 0.03, 0.03, 0.03, 0.03	0.296, 2.665, 1.184, 4.737	500, 1000, 1500, 2000	4

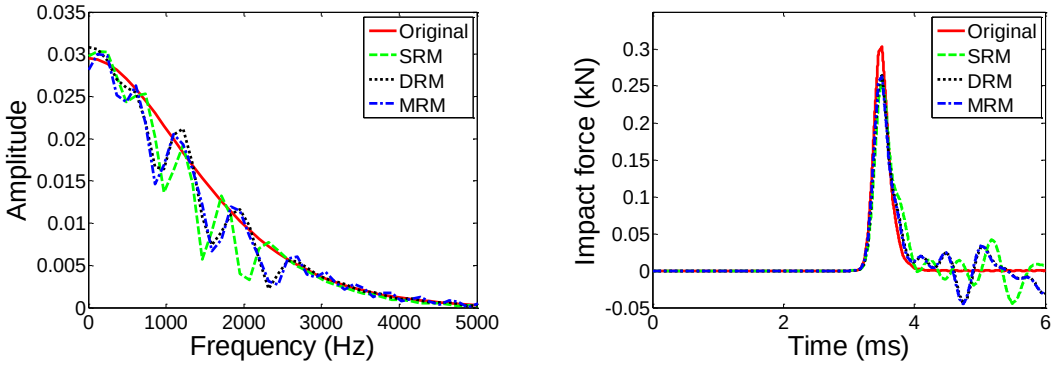

(a) (b)

FIG. 9. (a) Attenuation of frequency spectrum with different AMs. (b) Mitigation of impact force with different AMs.

Table 6. Maximum impact force with three different AM models.

Original (kN)	SRM (kN)	DRM (kN)	MRM (kN)
0.303	0.260	0.265	0.263

Figure 9(b) and Table 6 show that the maximum impact forces with the SRM, DRM, and MRM models are 0.260 kN, 0.265 kN, and 0.263 kN, respectively. Together with Fig. 9(a), it is clear that the mitigations of frequency spectrum and impact force with these three AM models are very close. This indicates that the performance of one MRM unit cell is similar to those of four SRM unit cells and two DRM unit cells. In addition, because the outer mass m_1 is used less, the mass of one MRM unit cell is less than that of two DRM unit cells, and the mass of two DRM unit cells is less than that of four MRM unit cells. Therefore, the MRM model with its fewer unit cells and lower structural mass is more effective than the SRM and DRM models, and the excellent performance of the MRM in mitigating impact waves is clear.

IV. THREE-DIMENSIONAL CRASH MODEL

Instead of the 1D impact wave model in Section III, we use a crash model here to study further how AMs mitigate impact force. The characteristics of an actual crash make it difficult to obtain the exact frequency spectrum of the impact force. Therefore, with the present crash model, we study how impact force is mitigated without knowing its frequency spectrum.

As shown in Fig. 10(a), we begin by establishing a 3D beam structure. The six

degrees of freedom at one end of the beam are constrained, while a rigid plate with an initial speed of 13.8 m/s horizontally impacts the other end of the beam. The beam structure is divided into parts 1, 2, and 3. The impact force at the end of part 2 is acquired as the output response, and the duration of the entire collision is 1 ms. We used the commercial software LSDYNA to conduct the study.

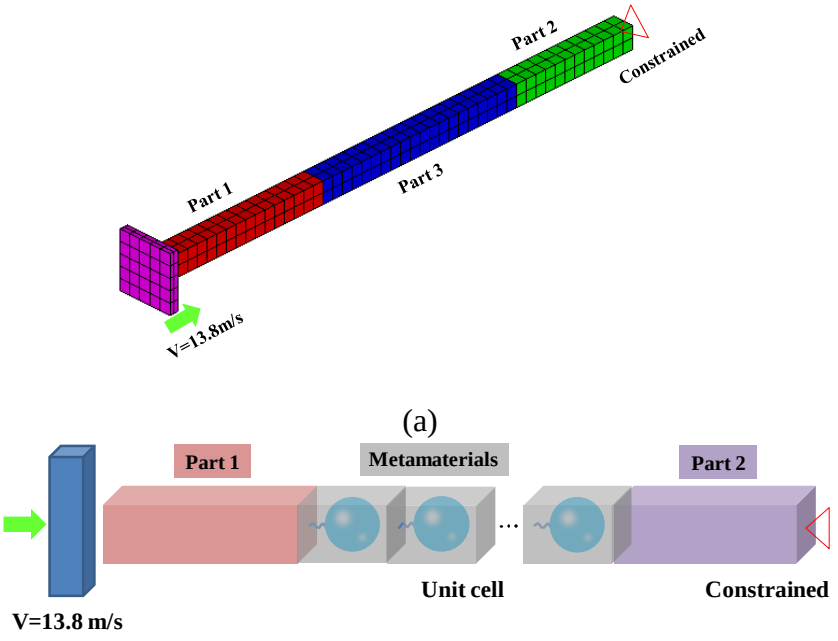

FIG. 10. (a) 3D crash model. (b) Schematic of crash model with AM.

Table 7. Parameters for two MRM unit cells, four DRM unit cells, and eight SRM unit cells.

	m_1, m_2, m_3, m_4, m_5 (kg)	k_2, k_3, k_4, k_5 (kN/mm)	ω_2, ω_4 (Hz)	N
MRM	0.01, 0.03, 0.03, 0.03, 0.03	1.184, 4.737, 2.665, 7.402	1000, 1500	2

	m_1, m_2, m_3, m_2, m_3 (kg)	k_2, k_3, k_2, k_3 (kN/mm)	ω_2, ω_2 (Hz)	N
DRM	0.01, 0.03, 0.03, 0.03, 0.03	1.184, 4.737, 2.665, 7.402	1000, 1500	4

	m_1, m_2, m_2, m_2, m_2 (kg)	k_2, k_2, k_2, k_2 (kN/mm)	ω_2, ω_2, ω_2, ω_2, (Hz)	N
SRM	0.01, 0.03, 0.03, 0.03, 0.03	1.184, 4.737, 2.665, 7.402	1000, 2000, 1500, 2500	8

As shown in Fig. 10(b), we insert an AM (SRM, DRM, or MRM) as part 3 to mitigate the impact force. First, we use eight SRM unit cells, four DRM unit cells, and two MRM unit cells to demonstrate the superior mitigation effect of the MRM. Second, we use 10 SRM unit cells, 10 DRM unit cells, and 10 MRM unit cells in the impact model to compare the performances of the three AM models with the same number of unit cells. The internal resonator masses of these AM models are all 0.03 kg, and the outer mass is 0.01 kg. Tables 7 and 8 give the parameters of all the AM models, and Fig. 11 and Table 9 present the corresponding results.

Table 8. Parameters of one unit cell in three different AM models.

	m_1, m_2, m_3, m_4, m_5 (kg)	k_2, k_3, k_4, k_5 (kN/mm)	ω_2, ω_4 (Hz)	N
SRM	0.01, 0.03, -, -	1.184, -, -, -	1000, -	10
DRM	0.01, 0.03, 0.003, -, -	1.184, 4.737, -, -	1000, -	10
MRM	0.01, 0.03, 0.003, 0.03, 0.03	1.184, 4.737, 2.665, 7.402	1000, 1500	10

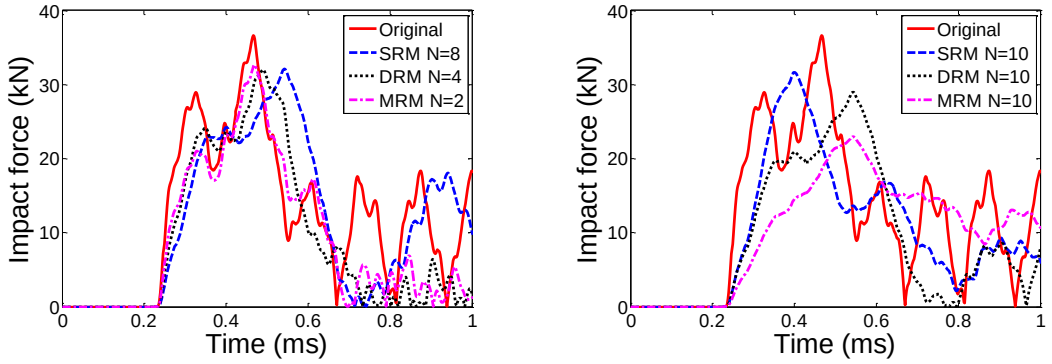

(a) (b)

FIG. 11. (a) Impact results with two MRM unit cells, four DRM unit cells, and eight SRM unit cells. (b) Impact force with each AM with 10 unit cells.

Table 9. Maximum impact forces with all AM models.

	Original	SRM		DRM		MRM	
N	——	8	10	4	10	2	10
Impact force (kN)	36.7	32.2	31.7	32.0	29.0	32.6	23.0

Figure 11 shows a considerable drop in the peak impact force at 0.24–0.67 ms for these three models, which implies that a high proportion of the impact stress wave passing through each AM is attenuated. This is due to the appearance of NEM for each of the SRM, DRM, and MRM AMs. Table 9 and Fig. 11(a) show that the maximum impact forces with eight SRM unit cells, four DRM unit cells, and two MRM unit cells are 32.2 kN, 32.0 kN, and 32.6 kN, respectively. Because these results are similar, we conclude that the MRM is more effective at attenuating the impact force given its weight and volume savings compared with the SRM and DRM. Table 9 and Fig. 11(b) show the crash results for these three AM models with 10 unit cells: the maximum impact forces with the SRM, DRM, and MRM models are 31.7 kN, 29.0 kN, and 23.0 kN, respectively. This shows strongly that the MRM achieves the best attenuation effect among these three AM models with the same volume.

V. CONCLUSION

In this work, a novel MRM was proposed. Theoretical analyses showed that the proposed MRM has multiple band gaps and a wider frequency range associated with NEM compared with an SRM and a DRM. Parametric studies based on a 1D impact wave model showed how the number of unit cells, the spring stiffnesses, and the resonator masses affect the mitigation of impact force. Furthermore, the 1D impact wave model and a 3D crash model showed that the MRM model always produces the maximum attenuation of the frequency spectrum and gives the minimum peak impact

force with the same number of unit cells. Compared with SRM and DRM, the MRM with a thin and light structure can give a better mitigation effect of the impact force and a wider attenuation region of the frequency spectrum.

[1] J. D. Baena, R. Marqués, F. Medina, and J. Martel, Physical Review B **20,** 1985 (2004).

[2] W. J. Padilla, A. J. Taylor, C. Highstrete, ., L. Mark, and R. D. Averitt, Physical Review Letters **96,** 107401 (2006).

[3] M. W. Klein, W. Martin, F. Nils, and L. Stefan, Optics Express **15,** 5238 (2007).

[4] C. M. Watts, X. Liu, and W. J. Padilla, Advanced Materials **24,** OP98 (2012).

[5] SobiaShoukat, ShakeelAhmed, M. A. Ashraf, A. A. Syed, and Q. A. Naqvi, Journal of Electromagnetic Waves & Applications **27,** 1127 (2013).

[6] Y. Ando, N. Miyamoto, K. Segawa, T. Kawata, and I. Terasaki, Phys.rev.b **601,** 1071114 (1999).

[7] D. Y. Chung, T. Hogan, P. Brazis, M. Rocci-Lane, C. Kannewurf, M. Bastea, C. Uher, and M. G. Kanatzidis, Science **287,** 1024 (2000).

[8] Z. H. Dughaish, Physica B Physics of Condensed Matter **322,** 205 (2002).

[9] B. Li, K. T. Tan, and J. Christensen, Physical Review B **95** (2017).

[10] B. Li, K. T. Tan, and J. Christensen, Journal Of Applied Physics **123** (2018).

[11] Y. Z. Wang, F. M. Li, and Y. S. Wang, International Journal of Mechanical Sciences **106,** 357 (2016).

[12] L. Xie, B. Xia, J. Liu, G. Huang, and J. Lei, International Journal of Mechanical Sciences **120** (2016).

[13] Z. Liu, X. Zhang, Y. Mao, Y. Y. Zhu, Z. Yang, C. T. Chan, and P. Sheng, Science **289,** 1734 (2000).

[14] J. Li and C. T. Chan, Physical Review E Statistical Nonlinear & Soft Matter Physics **70,** 055602 (2004).

[15] X. N. Liu, G. K. Hu, G. L. Huang, and C. T. Sun, Applied Physics Letters **98,** 509 (2011).

[16] R. Zhu, G. L. Huang, H. H. Huang, and C. T. Sun, Physics Letters A **375,** 2863 (2011).

[17] Z. C. He, E. Li, G. Wang, G. Y. Li, and Z. Xia, Acta Mechanica **227,** 1 (2016).

[18] E. Li, Z. C. He, and G. Wang, Computational Materials Science **122,** 72 (2016).

[19] H. B. A. Ba'Ba'A and M. Nouh, International Journal of Mechanical Sciences **122,** 341 (2017).

[20] B. Li and K. T. Tan, Journal Of Applied Physics **120** (2016).

[21] B. Li, S. Alamri, and K. T. Tan, Scientific Reports **7** (2017).

[22] S. Alamri, B. Li, and K. T. Tan, Journal Of Applied Physics **123** (2018).

[23] N. Cselyuszka, M. Sečujski, and V. Crnojević-Bengin, Physics Letters A **379,** 33 (2015).

[24] B. Assouar, M. Oudich, and X. Zhou, Comptes rendus - Physique **17,** 524 (2016).

[25] X. Wang, International Journal of Solids & Structures **51,** 1534 (2014).

[26] Z. Yang, H. Dai, N. Chan, G. Ma, and P. Sheng, Applied Physics Letters **96,** 041906 (2010).

[27] M. T. Islam and G. Newaz, Applied Physics Letters **100,** 509 (2012).

[28] C. J. Naify, C. M. Chang, G. Mcknight, and S. Nutt, Journal of Applied Physics **110,** 751 (2011).

[29] P. F. Pai, H. Peng, and S. Jiang, International Journal of Mechanical Sciences **79,** 195 (2014).

[30] E. Li, Z. He, G. Wang, and G. Liu, computational mechanics**,** 1 (2017).

[31] E. Li, Z. C. He, J. Y. Hu, and X. Y. Long, Computer Methods in Applied Mechanics and Engineering **324,** 128 (2017).
[32] Z. He, J. Hu, and E. Li, Computational Mechanics**,** 1 (2018).
[33] E. Li, Z. C. He, G. Wang, and Y. Jong, Advances in Engineering Software **121,** 167 (2018).
[34] E. Li, Z. C. He, G. Wang, and G. R. Liu, Computer Methods in Applied Mechanics and Engineering **333,** 421 (2018).
[35] X. Xiao, Z. He, E. Li, and A. Cheng, Mechanical Systems and Signal Processing **115,** 418 (2019).
[36] Z. Shu, Y. Leilei, and F. Nicholas, Physical Review Letters **102,** 194301 (2009).
[37] S. Gonella, A. C. To, and W. K. Liu, Journal of the Mechanics and Physics of Solids **57,** 621 (2009).
[38] K. Mikoshiba, J. M. Manimala, and C. Sun, Journal of Intelligent Material Systems and Structures **24,** 168 (2013).
[39] S. Yao, X. Zhou, and G. Hu, New Journal of Physics **10,** 043020 (2008).
[40] H. H. Huang and C. T. Sun, New Journal of Physics **11,** 013003 (2009).
[41] H. H. Huang, C. T. Sun, and G. L. Huang, International Journal of Engineering Science **47,** 610 (2009).
[42] J. M. Manimala, H. H. Huang, C. Sun, R. Snyder, and S. Bland, Engineering Structures **80,** 458 (2014).
[43] J. Zhou, Y. Cheng, H. Zhang, G. Huang, and G. Hu, Theoretical and Applied Mechanics Letters **5,** 196 (2015).
[44] X. Zhou, J. Wang, R. Wang, and J. Lin, Applied Physics A **122,** 427 (2016).
[45] A. Banerjee, R. Das, and E. Calius, Journal of Applied Physics **122,** 075101 (2017).
[46] Y. Liu, X. Su, and C. T. Sun, Journal of the Mechanics & Physics of Solids **74,** 158 (2015).
[47] K. T. Tan, H. H. Huang, and C. T. Sun, Applied Physics Letters **101,** 3966 (2012).
[48] K. T. Tan, H. H. Huang, and C. T. Sun, International Journal of Impact Engineering **64,** 20 (2014).